Monthly Notices
of the
ROYAL ASTRONOMICAL SOCIETY

MNRAS **445,** 1288–1298 (2014) doi:10.1093/mnras/stu1851

Multiwavelength observations of the black hole transient Swift J1745−26 during the outburst decay

E. Kalemci,[1⋆] M. Özbey Arabacı,[2] T. Güver,[3] D. M. Russell,[4,5] J. A. Tomsick,[6] J. Wilms,[7] G. Weidenspointner,[8,9] E. Kuulkers,[10] M. Falanga,[11] T. Dinçer,[1] S. Drave,[12] T. Belloni,[13] M. Coriat,[14] F. Lewis[15,16] and T. Muñoz-Darias[17]

[1]*Faculty of Engineering and Natural Sciences, Sabancı University, Orhanlı-Tuzla, 34956 Istanbul, Turkey*
[2]*Physics Department, Middle East Technical University, 06530 Ankara, Turkey*
[3]*Astronomy and Space Sciences Department, Istanbul University, 34119 Istanbul, Turkey*
[4]*New York University Abu Dhabi, PO Box 129188, Abu Dhabi, United Arab Emirates*
[5]*Instituto de Astrofisica de Canarias, C/Via Láctea s/n, E-38205 La Laguna, Tenerife, Spain*
[6]*Space Sciences Laboratory, 7 Gauss Way, University of California, Berkeley, CA 94720-7450, USA*
[7]*Dr Karl-Remeis-Sternwarte and Erlangen Centre for Astroparticle Physics, Friedrich Alexander Universität Erlangen-Nürnberg, Sternwartstr. 7, D-96049 Bamberg, Germany*
[8]*European X-ray Free Electron Laser Facility GmbH, Albert-Einstein-Ring 19, D-22761 Hamburg, Germany*
[9]*Max Planck Institut für Extraterrestrische Physik, Giessenbachstrasse 1, D-85748 Garching, Germany*
[10]*European Space Agency, European Space Astronomy Centre, PO Box 78, E-28691 Villanueva de la Canada, Madrid, Spain*
[11]*International Space Science Institute (ISSI), Hallerstrasse 6, CH-3012 Bern, Switzerland*
[12]*School of Physics and Astronomy, Faculty of Physical Sciences and Engineering, University of Southampton, University Road, Southampton SO17 1BJ, UK*
[13]*INAF – Osservatorio Astronomico di Brera, Via E. Bianchi 46, I-23807 Merate, Italy*
[14]*Department of Astronomy, University of Cape Town, Private Bag X3, Rondebosch 7701, South Africa*
[15]*Faulkes Telescope Project, University of South Wales, Pontypridd CF37 1DL, UK*
[16]*Astrophysics Research Institute, Liverpool John Moores University, IC2, Liverpool Science Park, 146 Brownlow Hill, Liverpool L3 5RF, UK*
[17]*Department of Physics, Astrophysics, University of Oxford, Keble Road, Oxford OX1 3RH, UK*

Accepted 2014 September 4. Received 2014 August 20; in original form 2014 June 9

ABSTRACT

We characterized the broad-band X-ray spectra of Swift J1745−26 during the decay of the 2013 outburst using *INTEGRAL* ISGRI, JEM-X and *Swift* XRT. The X-ray evolution is compared to the evolution in optical and radio. We fit the X-ray spectra with phenomenological and Comptonization models. We discuss possible scenarios for the physical origin of an ∼50 d flare observed both in optical and X-rays ∼170 d after the peak of the outburst. We conclude that it is a result of enhanced mass accretion in response to an earlier heating event. We characterized the evolution in the hard-X-ray band and showed that for the joint ISGRI–XRT fits, the e-folding energy decreased from 350 to 130 keV, while the energy where the exponential cut-off starts increased from 75 to 112 keV as the decay progressed. We investigated the claim that high-energy cut-offs disappear with the compact jet turning on during outburst decays, and showed that spectra taken with HEXTE on *RXTE* provide insufficient quality to characterize cut-offs during the decay for typical hard-X-ray fluxes. Long *INTEGRAL* monitoring observations are required to understand the relation between the compact jet formation and hard-X-ray behaviour. We found that for the entire decay (including the flare), the X-ray spectra are consistent with thermal Comptonization, but a jet synchrotron origin cannot be ruled out.

Key words: stars: black holes – stars: individual: Swift J174510.8−2624 – X-rays: binaries.

1 INTRODUCTION

Galactic black hole transients (GBHTs) are excellent laboratories to study the complex relation between the jet and the accretion environment in X-ray binaries as the outbursts evolve on time-scales of months, allowing detailed investigation of the properties of accretion states (traced by X-ray spectral and timing properties) together with the properties of jets traced by the radio, and optical/infrared (OIR) emission.

The evolution of accretion states throughout an outburst is best described by the hardness–intensity diagram (HID; Homan et al.

⋆E-mail: ekalemci@sabanciuniv.edu

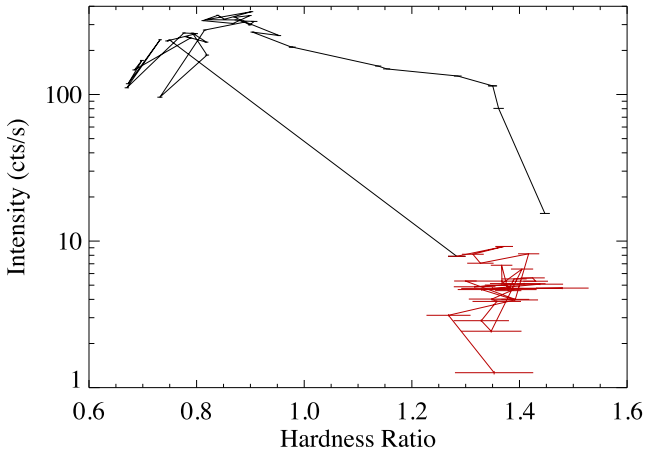

Figure 1. HID of Swift J1745−26 obtained using the *Swift* XRT data only. The hardness ratio is defined as ratio of counts in 2.5–10 and 1–2.5 keV bands and the intensity is the count rate in 1–10 keV band. Red data points represent the observations used in this work.

2001; Belloni 2010). The HID of Swift J1745−26 is given in Fig. 1. At the start of a typical outburst, the GBHT is in the hard state (HS), the lower-right side of the HID. In this state, the X-ray spectrum is dominated by a hard, power-law-like component, historically associated with Compton scattering of soft photons by a hot electron corona. Weak emission from a cool, optically thick, geometrically thin disc (modelled by a multitemperature blackbody; Makishima et al. 1986) may also be observed. The variability is strong (typically >20 per cent fractional rms amplitude). As the X-ray flux increases, the GBHT usually makes a transition to the soft state (upper-left side of the HID) in which the X-ray spectrum is dominated by the optically thick accretion disc. At the end of outbursts, sources go back to the HS as the X-ray flux decreases. There are also intermediate states occurring during transitions between the soft and the hard states (see McClintock & Remillard 2006; Belloni 2010 for details of spectral states of GBHTs).

In some cases, the evolution of spectral states during an outburst does not follow the usual pattern in the HID. The source can stay in the HS throughout the outburst or make a transition to a hard intermediate state while never fully entering the soft state. These are called 'failed outbursts' (Brocksopp, Bandyopadhyay & Fender 2004; Russell et al. 2013a; Soleri et al. 2013). The HID of Swift J1745−26 given in Fig. 1 is a typical HID for a failed outburst (see Capitanio et al. 2009; Ferrigno et al. 2012; Soleri et al. 2013, for other examples of failed outburst HIDs).

Contemporaneous multiwavelength observations of GBHTs in OIR and radio show that the behaviour of the jets are closely related to X-ray spectral states. Steady, compact jets are observed in the HS (Corbel et al. 2000; Fender 2001, 2010; Fender & Gallo 2014). The typical spectral energy distributions (SEDs) in the HS show a flat or inverted power law at radio frequencies that breaks, at near- to mid-infrared wavelengths, to a second power law with negative spectral index. Such an emission profile is consistent with emission from a compact, conical jet (Blandford & Konigl 1979; Hjellming & Johnston 1988). On the other hand, the radio emission from the jet is quenched in the soft state (Corbel & Fender 2002; Russell et al. 2011). During the transition to the soft state in the outburst rise, bright relativistic flares with optically thin radio spectra are sometimes observed (see Fender & Gallo 2014, and references therein).

Two important aspects of the relation between X-ray spectral and timing properties and the jets are understanding the conditions in the accretion environment for the formation of compact jets (Kalemci et al. 2013, and references therein), and whether jets affect the X-ray spectral and timing properties by altering the accretion environment. One way of achieving these objectives is characterizing the X-ray spectral evolution along with the OIR and radio evolution during outburst decays because the jet emission that is quenched during the soft state turns back on as the source makes a transition to the HS.

Such multiwavelength characterization during the outburst decays reveal OIR flares (also called 'secondary maxima') when the source is back in the HS with the X-ray spectrum close to its hardest level (Buxton & Bailyn 2004; Kalemci et al. 2005, 2013; Coriat et al. 2009; Russell et al. 2010; Buxton et al. 2012; Dinçer et al. 2012). In the 2011 decay of GX 339−4, simultaneous radio and OIR observations show that the OIR flare corresponds to a transition in radio from optically thin to optically thick emission (Corbel et al. 2013a,b). Moreover, the SEDs created from data during the OIR flares of 4U 1543−47 (Buxton & Bailyn 2004; Kalemci et al. 2005) and XTE J1550−564 (Jain et al. 2001; Russell et al. 2010) are consistent with emission from a compact jet. A study by Kalemci et al. (2013) showed that the multiwavelength behaviour of most GBHTs that undergo a soft to hard state transition during the outburst decay are similar such that a compact, steady jet is formed 6–15 d after the initial changes in timing properties, and the jet manifests itself either as an OIR flare, and/or radio emission with flat to inverted spectrum. Alternative explanations for these OIR flares exist, such as the synchrotron emission from a hot accretion flow (Poutanen & Veledina 2013; Veledina, Poutanen & Vurm 2013) and irradiation-induced secondary mass accretion which could explain the secondary OIR flares with simultaneous X-ray flares (Kalemci et al. 2013).

To understand the effects of the jet on the X-ray spectral properties, we started a programme with the *INTEGRAL* observatory to characterize the GBHTs at high energies when compact jets are present (or while they form). Thermal Comptonization models that are often invoked to explain the high-energy behaviour of GBHTs predict a cut-off in the X-ray spectrum at a few hundred keVs (Gilfanov 2010). While such cut-offs are observed commonly in many GBHTs, in some cases these cut-offs disappear after the jets turn on (such as in 4U 1543−47; Kalemci et al. 2005), or are not present at all while the jets are present (H1743−322 during the 2003 decay, Kalemci et al. 2006a; GX 339−4 during the 2005 outburst, Kalemci et al. 2006b; XTE J1720−318, Cadolle Bel et al. 2004; GRO J1655−40 during the 2005 decay, Caballero García et al. 2007, but also see Joinet, Kalemci & Senziani 2008). This disappearance could be interpreted as the jet changing the electron energy distribution and hardening the X-ray spectrum.

Synchrotron emission from compact jets may also be contributing to hard X-rays (Markoff, Falcke & Fender 2001; Markoff, Nowak & Wilms 2005; Maitra et al. 2009; Russell et al. 2010), and both Comptonization and jet models can fit the spectra equally well (Nowak et al. 2011). According to Pe'er & Markoff (2012), a distinct feature of synchrotron radiation at hard X-rays would be a photon index of around 1.5 before a gradual break in the spectrum at ∼10 keV caused by rapid cooling of electrons. Characterizing properties of spectral breaks at hard X-rays therefore is important to test predictions of jet models, especially when these models incorporate detailed electron acceleration mechanisms.

Using HEXTE on *RXTE*, Miyakawa et al. (2008) investigated the relation between the cut-off energy (from the fits with cut-off power

law) and several other spectral parameters from all HS observations of GX 339−4, and found an inverse correlation between the cut-off energy and luminosity for the bright HS observations. The statistics were not good enough to constrain the evolution of the cut-off parameters for the fainter observations. Motta, Belloni & Homan (2009) utilized *INTEGRAL* ISGRI and HEXTE together and investigated the evolution of the cut-off energy from the HS to the hard intermediate state in the rising phase of the outburst of GX 339−4 during the 2006/2007 outburst. Similar to findings of Miyakawa et al. (2008), the cut-off energy decreased with increasing flux, but it reversed the trend and increased again with the softening in the hard-intermediate state. While the cause of this behaviour is not clear, obtaining the evolution of spectral breaks during the outburst decay, and comparing with the outburst rise could help us to uncover the reason. Since the hard-X-ray fluxes during the outburst decays are lower, dedicated observing programmes with *INTEGRAL* are required for such investigation.

Within our *INTEGRAL* programme, we first observed XTE J1752−223 with *INTEGRAL*, *Swift* and *RXTE* during its 2012 outburst decay (Chun et al. 2013). The observation took place a few days before the detection of the compact core with the Very Long Baseline Array (VLBA). To increase the statistics of the X-ray spectra at high energy, we combined all available ISGRI data, and the resulting spectrum required a break in the hard-X-ray spectrum. As a continuation of our observing programme with *INTEGRAL*, we triggered on Swift J1745−26 during its decay in 2013. We also obtained data from *INTEGRAL* revolutions before and after our observation.

1.1 Swift J1745−26

Swift J1745−26 (Swift J174510.8−2624) was discovered by the BAT instrument on board the *Swift* satellite on 2012 September 16 (MJD 56186.39; Cummings et al. 2012). It was subsequently detected by the *Swift* XRT (Sbarufatti et al. 2012) and *INTEGRAL* (Vovk et al. 2012). The infrared counterpart was identified by Rau et al. (2012). Based on the X-ray spectral and timing properties, Swift J1745−26 is reported to be a GBHT (Belloni et al. 2012; Tomsick, Del Santo & Belloni 2012). Further evidence for the nature of the source comes from optical observations that reveal a broad, double-peaked Hα emission line whose properties resemble those typically seen in other black hole sources in outburst (de Ugarte Postigo et al. 2012; Muñoz-Darias et al. 2013).

Swift J1745−26 is also detected in radio both with the Karl G. Jansky Very Large Array (VLA; Miller-Jones & Sivakoff 2012) and at the Australia Telescope Compact Array (ATCA; Corbel et al. 2012). The spectral index of radio observations during the initial HS is consistent with optically thick synchrotron emission from a partially self-absorbed compact jet (Corbel et al. 2012). Curran et al. (2014) present detailed analysis of radio data from ATCA, VLA and Karoo Array Telescope monitoring observations of Swift J1745−26 until MJD 56380. After the initial HS rise, the source stayed in the hard intermediate state until MJD 56270 based on X-ray spectral and timing properties (Belloni et al. 2012; Grebenev & Sunyaev 2012) and also radio emission properties (Curran et al. 2014). Detailed *Swift* and *INTEGRAL* analysis of the outburst rise can be found in Del Santo et al. (in preparation).

Due to the proximity of the source to the Sun, the source could not be observed between MJD 56270 and MJD 56288 with *Swift* BAT, and the first pointed observation of the source with *Swift* XRT after the gap was on MJD 56334. As shown in fig. 1 of Curran et al. (2014), the system was in the hard intermediate state at MJD 56250 as indicated by the inverted spectrum radio emission. The BAT flux shows an increasing trend after this date, indicating that the spectrum remained hard until the start of the Sun gap on MJD 56270. After a gap of 18 d, the BAT light curve before the break smoothly connects to the light curve after the break. The radio spectrum taken on MJD 56304 and the X-ray spectra on MJD 56334 (Sbarufatti et al. 2013) show that the source is in the HS after the break. This can also be seen in the HID given in Fig. 1, where the red data points represent observations analysed in this work. While we cannot rule out the possibility that the source entered the soft state between MJD 56270 and MJD 56304, the trends in the *Swift* BAT light curve and the radio evolution indicate a 'failed' outburst. We note that, while the properties of the source are consistent with the definition of failed outbursts, the outburst certainly did not fail in terms of brightness, and had reached close to a Crab during the initial rise (Sbarufatti et al. 2012).

Finally, the source exhibited a secondary flare after MJD 56380 in optical and X-rays (Russell et al. 2013b). Thanks to the large field of view of *INTEGRAL* and the position of the source in the Galactic bulge, we were able to analyse *INTEGRAL* data from several revolutions to characterize the high-energy behaviour of the source over 70 d during its decay. In this paper, we first present the X-ray evolution of the source using both *INTEGRAL*, and *Swift*. Then we discuss the secondary flare observed in both optical and X-ray and compare this flare with the secondary OIR flares observed in GBHTs.

2 OBSERVATIONS AND ANALYSIS

2.1 X-ray observations

A summary plot of all multiwavelength observations during the decay can be found in Fig. 2. The source has been covered very well with *Swift* and *INTEGRAL*. Our analysis includes *Swift* data between MJD 56334.23 and MJD 56435.59, and *INTEGRAL* data between MJD 56334.0 and MJD 56397.8. The details of the *INTEGRAL* revolutions we utilized and simultaneous *Swift* ObsIDs are given in Table 1.

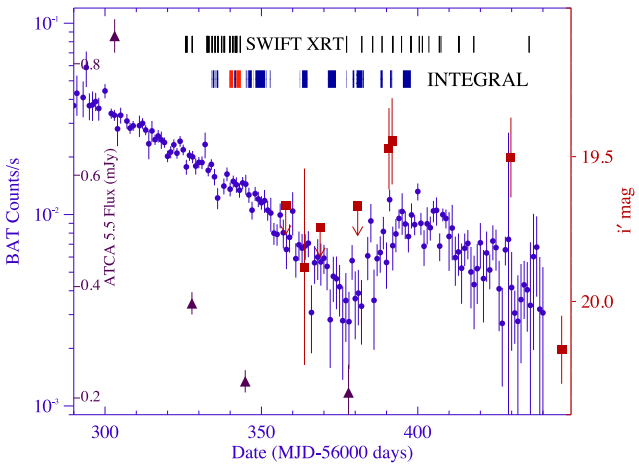

Figure 2. Multiwavelength observations used in this work. Blue filled circles represent *Swift* BAT count rate, filled orange squares are i' magnitudes (from FTS and RTT 150), purple filled triangles are ATCA radio fluxes at 5.5 GHz. The black short lines at the top represent the times of *Swift* pointed observations. The regions below the *Swift* observations are the times for which the source is within 10° of the *INTEGRAL* pointing direction. The lighter region represents dedicated *INTEGRAL* observations (PI Kalemci).

Table 1. *INTEGRAL* observation details.

ISGRI rev[a]	Dates MJD−56000	*Swift* ObsID[b]	ISGRI exposure (ks)	Avg. offset[c]
1261	334.0–335.0	00032700005	61.0	3°.93
1262	335.3–336.2	00032700007	48.0	5°.19
1263	339.7–340.9	000327000010	103.7	4°.18
1264	341.3–343.4	000327000013	151.9	4°.82
1265	345.0–346.9	–	35.0	6°.18
1266	347.3–349.8	–	20.8	5°.31
1267	351.0–352.9	–	29.2	5°.94
1271	362.2–364.8	–	27.3	6°.05
1274	371.2–373.2	–	22.7	6°.17
1276	377.2–379.7	00533836047	104.0	5°.27
1277	380.2–382.7	–	184.2	6°.34
1279	388.0–388.8	00032700017	61.8	4°.85
1280	391.1–391.8	00032700018	44.9	5°.13
1282	395.2–397.8	00533836049	129.5	8°.50

Note: [a]ISGRI revolution.
[b]*Swift* observation within the given revolution.
[c]Average offset of ISGRI pointings.

2.2 Spectral extraction with *Swift* XRT, *INTEGRAL* ISGRI and JEM-X

The *Swift* XRT observations used in this study are shown in Table 2. All data were processed following the standard procedures and using the XRTPIPELINE v.0.12.8. Since the source flux varies significantly, the whole sample of pointings contain both windowed timing (WT) mode and photon counting (PC) mode data. In order to minimize the effects of photon pile-up, we followed the method outlined in Reynolds & Miller (2013) and created source selection regions based on the observed count rate. The background region was selected from an annulus with an inner and outer radius of 70 and 100 arcsec, respectively, from the source centroid. Events were selected with grades 0–2 and 0–12 for WT and PC mode data, respectively. The appropriate response matrix files, swxwt0to2s6_20010101v014.rmf for the WT mode and swxpc0to12s6_20010101v013.rmf for the PC mode, were obtained from HEASARC CALDB. The auxiliary response matrix files were created using the HEASOFT tool *xrtmkarf* and the exposure map created by the *xrtexpomap*. Finally, we grouped all the spectra to have at least 50 counts per spectral bin. After the pile-up mitigating procedure, the PC mode observations resulted in a spectrum with few energy bins and large errors, and therefore are not used in this work.

The *INTEGRAL* data were reduced and analysed using the standard Off-line Scientific Analysis (OSA) software package (v.10) released by the ISDC (Courvoisier et al. 2003) for each revolution. The *INTEGRAL* revolutions last ∼3 d, and within revolutions sky regions are observed with 30–60 min individual pointings with a special dither pattern to minimize noise in mosaic images obtained by combining images from individual pointings.

For JEM-X, we combined images in a single mosaic per revolution in order to reach the highest sensitivity for JEM X-1 and JEM X-2 separately. The spectra were extracted from the each combined mosaic image over an energy range of 3–35 keV corresponding to 16 channels. After comparing the quality of spectra, we have decided to use only JEM X-1 data. In the case of IBIS/ISGRI, the standard procedure was used to extract the spectra and rebin the response matrix to 50 bins. Then we used *spe_pick* tool to obtain

Table 2. *Swift* XRT-only fit results.

Swift ObsID	Date[a]	Fits with free N_H			Fits with N_H fixed			
		N_H[b]	Γ	T_{in}	Γ	T_{in}	Flux[c]	Norm[d]
00032700005	334.2	2.12 ± 0.23	1.60 ± 0.07	0.10 ± 0.02	1.62 ± 0.03	0.11 ± 0.02	7.61 ± 0.10	>1.07E+06
00032700007	336.1	2.08 ± 0.24	1.68 ± 0.08	0.11 ± 0.02	1.72 ± 0.03	0.11 ± 0.01	6.04 ± 0.09	>1.64E+06
00032700008	337.2	2.14 ± 0.27	1.64 ± 0.08	0.11 ± 0.03	1.65 ± 0.04	0.12 ± 0.02	6.81 ± 0.08	>2.41E+05
00032700009	338.0	1.88 ± 0.15	1.53 ± 0.06	0.07 ± 0.03	1.61 ± 0.04	0.13 ± 0.03	6.90 ± 0.08	>1.15E+05
00032700010	339.9	2.08 ± 0.30	1.58 ± 0.08	0.12 ± 0.03	1.61 ± 0.04	0.13 ± 0.02	6.22 ± 0.09	>3.00E+05
00032700011	341.6	2.44 ± 0.27	1.70 ± 0.07	0.14 ± 0.01	1.64 ± 0.04	0.14 ± 0.02	6.12 ± 0.07	>2.52E+05
00032700012	340.8	2.41 ± 0.28	1.69 ± 0.09	0.12 ± 0.01	1.62 ± 0.04	0.12 ± 0.01	6.14 ± 0.09	>1.27E+06
00032700013	342.0	2.26 ± 0.26	1.68 ± 0.08	0.12 ± 0.02	1.66 ± 0.04	0.12 ± 0.02	6.39 ± 0.09	>6.83E+05
00032700014	343.2	2.22 ± 0.27	1.64 ± 0.07	0.12 ± 0.02	1.63 ± 0.04	0.12 ± 0.02	6.16 ± 0.06	>3.52E+05
00533686047	377.2	1.64 ± 0.23	1.49 ± 0.13	–	1.59 ± 0.11	0.17 ± 0.07	2.19 ± 0.07	>2.10E+04
00032700017	388.6	2.76 ± 0.55	1.85 ± 0.19	0.10 ± 0.02	1.68 ± 0.08	0.10 ± 0.02	2.70 ± 0.09	>1.59E+06
00032700018	391.9	2.29 ± 0.52	1.69 ± 0.17	0.10 ± 0.04	1.67 ± 0.08	0.11 ± 0.03	3.39 ± 0.11	>3.14E+05
00533836048	392.1	2.36 ± 0.55	1.68 ± 0.16	0.12 ± 0.03	1.64 ± 0.08	0.13 ± 0.03	3.57 ± 0.09	>1.18E+05
00032700019	394.8	2.21 ± 0.46	1.63 ± 0.15	0.10 ± 0.03	1.63 ± 0.07	0.11 ± 0.03	4.14 ± 0.10	>6.08E+05
00533836049	397.8	3.28 ± 0.66	1.86 ± 0.15	0.15 ± 0.02	1.63 ± 0.07	0.16 ± 0.03	4.31 ± 0.12	>2.10E+04
00032700020	397.9	1.92 ± 0.33	1.59 ± 0.13	0.08 ± 0.06	1.67 ± 0.07	0.12 ± 0.06	4.47 ± 0.12	>4.50E+05
00032700021	400.5	2.66 ± 0.49	1.74 ± 0.14	0.11 ± 0.02	1.62 ± 0.06	0.11 ± 0.02	4.46 ± 0.10	>9.16E+05
00533836050	401.5	2.74 ± 0.55	1.76 ± 0.15	0.14 ± 0.03	1.63 ± 0.07	0.13 ± 0.04	4.55 ± 0.11	>4.06E+05
00032700022	403.6	2.37 ± 0.88	1.62 ± 0.25	0.11 ± 0.07	1.58 ± 0.11	0.13 ± 0.05	4.32 ± 0.19	>5.39E+05
00032700023	406.9	2.84 ± 0.53	1.77 ± 0.16	0.11 ± 0.02	1.60 ± 0.07	0.11 ± 0.02	4.28 ± 0.12	>6.76E+05
00533836051	407.4	2.35 ± 0.49	1.75 ± 0.16	0.11 ± 0.02	1.70 ± 0.08	0.11 ± 0.02	3.92 ± 0.11	>5.14E+05
00533836052	413.1	2.23 ± 0.47	1.64 ± 0.16	0.09 ± 0.04	1.64 ± 0.07	0.10 ± 0.03	3.54 ± 0.09	>5.00E+05
00533836053	417.4	2.20 ± 0.00	1.60 ± 0.10	0.17 ± 0.04	1.60 ± 0.10	0.17 ± 0.04	3.06 ± 0.10	>1.43E+05
00533836057	435.6	3.14 ± 1.08	2.01 ± 0.32	0.08 ± 0.06	1.79 ± 0.10	–	3.12 ± 0.13	–

Note: [a]MJD−56000.
[b]In units of 10^{22} atoms cm^{-2}.
[c]1–12 keV flux in units of 10^{-10} erg cm^{-2} s^{-1}.
[d]Lower limit of normalization of *diskbb* component.

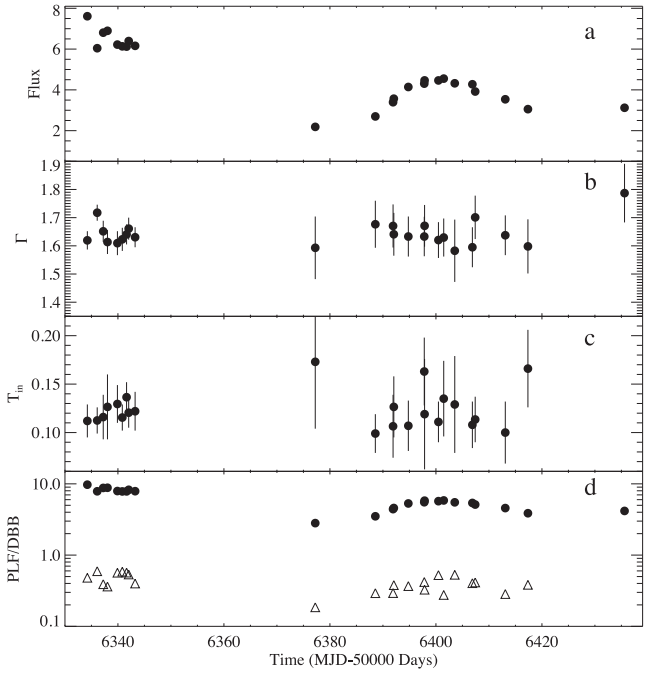

Figure 3. Plot of X-ray spectral parameters of *Swift* XRT data only, fitted with a power-law+diskbb model, interstellar absorption (tbabs) with $N_{\rm H}$ fixed to 2.18×10^{22} cm^{-2}. (a): 1–12 keV flux in units of 10^{-10} erg cm^{-2} s^{-1}. (b): power-law photon index, (c): diskbb inner disc temperature in keV, (d): PLF (filled circle) is the power-law flux and DBB (triangle) is the diskbb flux in units of 10^{-10} erg cm^{-2} s^{-1} in 1–12 keV band.

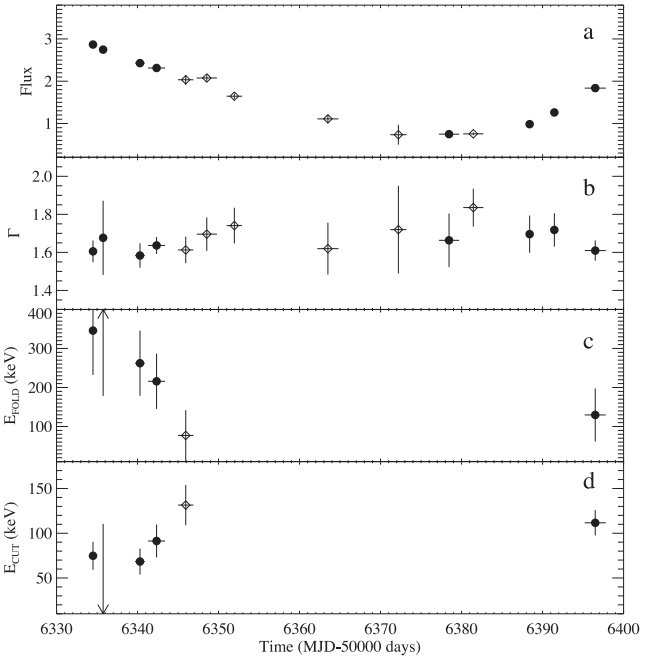

Figure 4. Evolution of spectral fit parameters for the fits with *highecut*power* model. Filled circles are joint fits to *INTEGRAL* ISGRI and *Swift* XRT (therefore the model also includes *diskbb*), and open diamonds are fits to only ISGRI spectra. (a): 13–200 keV flux in units of 10^{-9} erg cm^{-2} s^{-1}. (b): photon index. (c): folding energy and (d): cut-off energy of the *highec* model, respectively.

average spectrum of the source for each revolution for 18–350 keV energy range.

2.3 X-ray spectral analysis

We first fitted *Swift* XRT and *INTEGRAL* ISGRI spectra separately. For the *Swift* XRT fits, we started with interstellar absorption (*tbabs* in XSPEC) and a power law. We used cross-sections of Verner et al. (1996) and abundances of Wilms, Allen & McCray (2000) for the interstellar absorption and left $N_{\rm H}$ as a free parameter initially. We observed significant residuals at energies less than 2 keV. We added a multicolour disc blackbody (*diskbb* in XSPEC; Makishima et al. 1986) which resulted in fits with acceptable reduced χ^2 values. The results of the fits are tabulated in Table 2.[1]

For the initial, high-flux, high-quality spectra between MJD 55633.4 and MJD 55644.3, we realized that fits result in a small scatter of $N_{\rm H}$ values around an average of 2.18×10^{22} atoms cm^{-2}. Lower quality spectra showed large scatter in $N_{\rm H}$ that correlated with disc fit parameters. Since it is unlikely that $N_{\rm H}$ varies more than 20 per cent within time-scale of days, we fixed its value to 2.18×10^{22} atoms cm^{-2} and performed the fits again. The results show a smooth evolution of X-ray spectral parameters as seen in Fig. 3 and in Table 2.

For the *INTEGRAL* observations, we first fitted the ISGRI data from individual revolutions. We started with a power law, and added a high-energy cut-off component (*highecut* in XSPEC) and test if addition of the cut-off significantly improves the χ^2. If an *F*-test results in chance probability less than 0.001, we used the fit with the cut-off. The fit results are summarized in Table 4 and some of the fit parameters are plotted in Fig. 4.

Finally, we applied joint fits to the *Swift* XRT, *INTEGRAL* ISGRI and JEM-X for observations with concurrent data (Table 1). We started with a model that consists of power law and multicolour disc blackbody components with interstellar absorption. Similar to ISGRI-only fits, we add a high-energy cut-off and check the improvement in χ^2. If an *F*-test results in chance probability less than 0.001, we used the fit with the cut-off.

We also applied thermal and hybrid Comptonization models to the joint spectra. In the *compps* model (Poutanen & Svensson 1996), blackbody photons are Compton up-scattered from a spherical corona with uniform optical depth τ_y and electron temperature $kT_{\rm e}$. In our fits, the blackbody temperature is fixed to the *diskbb* inner temperature $T_{\rm in}$. We kept all other parameters at default values. The fits cannot constrain the reflection fraction.

Finally, we tried the *eqpair* model (Coppi 1999) to be able to assess the presence of non-thermal electron population. The *eqpair* model assumes a spherical plasma of electrons, positrons and soft photons. The resulting emission is determined by the compactness parameter $l = L\sigma_{\rm T}/Rm_{\rm e}c^3$, where L is power, R is the radius of the spherical plasma and $\sigma_{\rm T}$ is the Thomson cross-section. The model allows hybrid electron plasmas, thermal and non-thermal electron energy distributions together. Following Coppi (1999), we fixed the soft-photon compactness $l_{\rm s}$ to 1, and fit our data with a minimum set of free parameters. The temperature of seed photons are fixed to the inner disc temperature of the *diskbb* component. The fit results for Comptonization models are summarized in Table 5. An example fit is shown in Fig. 5.

[1] All errors in the figures and in tables correspond to $\Delta\chi^2$ of 2.706.

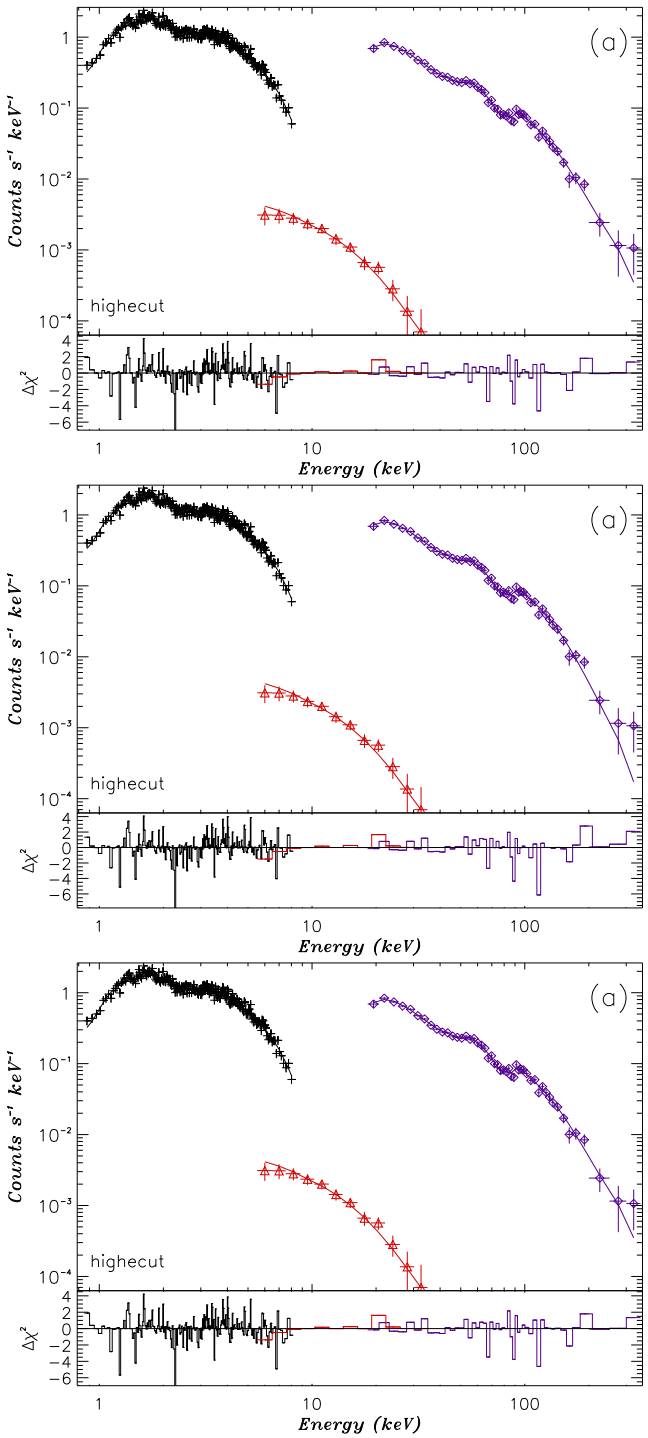

Figure 5. Fits to joint *Swift* XRT (crosses), *INTEGRAL* ISGRI (diamonds) and JEM-X (triangles) spectra for revolution 1263. Fits are with (a): *highecut*, (b): *comps* and (c): *eqpair* model.

2.4 Radio and optical data

During the decay, the source was also monitored in radio and in optical. There were four radio observations with the ATCA, and for all those observations the radio spectra are consistent with being flat to inverted, indicating presence of compact jets (Curran et al. 2014).

Optical observations were acquired using the Faulkes Telescope South (FTS; located at Siding Spring, Australia) as part of a monitoring campaign of ∼30 low mass X-ray binaries with the Faulkes Telescopes (Lewis et al. 2008). Three filters were used, Sloan Digital Sky Survey i', Bessell R and Bessell V. Bias subtraction and flat-fielding were performed via the automatic pipelines. For flux calibration procedures, see Muñoz-Darias et al. (2013). The magnitudes in each band are given in Table 3. We also take one i'-band magnitude measured on MJD 56446 taken at Turkish National Observatory with Russian Turkish Telescope RTT150 reported in Grebenev et al. (2014).

Table 3. Optical magnitudes.

Date	i'	R	V
56357.8	>19.67	>20.75	>19.73
56363.8	19.88 ± 0.34	20.92 ± 0.35	>21.13
56368.8	>19.74	20.67 ± 0.24	>21.19
56380.8	>19.67	>20.83	>20.39
56390.8	19.47 ± 0.14	20.72 ± 0.25	>20.83
56391.8	19.45 ± 0.15	20.45 ± 0.21	21.58 ± 0.48
56429.8	19.50 ± 0.14	20.20 ± 0.13	22.94 ± 0.55
56441.8	>18.67	>20.36	21.04 ± 0.55
56451.8	>18.98	>20.49	>21.97
56537.4	>20.78	–	>21.26
56446[a]	20.07 ± 0.12	–	–

Note: [a]From Grebenev, Prosvetov & Burenin (2014).

3 RESULTS

3.1 Soft-X-ray evolution with *Swift* XRT

As mentioned earlier, leaving $N_{\rm H}$ free results in highly scattered and correlated $N_{\rm H}$ and *diskbb* parameters. In some cases, the *diskbb* flux changes by an order of magnitude within a day. After fixing the $N_{\rm H}$, a smooth evolution of X-ray spectral fit parameters is observed (Fig. 3).

A soft *diskbb* component is required statistically in the fits; however, its parameters are not very well determined, especially the normalization. The 90 per cent confidence lower limits on the *diskbb* normalizations are given in Table 2 along with other important fit parameters. The minimum normalizations typically are larger than a few times 10^5, and the lowest we measure is 10^4. While the quality of the data is not good enough to place strong constraints on the inner disc radius, for typical black hole masses and distances, these minimum normalization values indicate large inner disc radii.

The 1–12 keV X-ray flux decreases from 8×10^{-10} to 2×10^{-10} erg cm^{-2} s^{-1} in ∼43 d before showing a flare. The flare lasts for approximately 40 d. As seen in Fig. 2, the flare occurs in both soft and hard X-rays. The flare causes an increase of flux in both *diskbb* and power-law flux, and the photon indices remain remarkably constant even though the soft-X-ray flux more than doubles during the flare.

3.2 Hard-X-ray evolution and joint fits

The evolution of the hard-X-ray flux with BAT is shown in Fig. 2, and the evolution of the spectral fit parameters of *INTEGRAL* ISGRI data only are given in Table 4. We were able to search and detect cut-offs in the ISGRI data for revolutions with high flux (1261–1265), and also during the final revolution (1282) for which the source was in the field of view of *INTEGRAL*. For revolution 1282, the statistical quality of the spectrum is better than for revolutions

Table 4. ISGRI-only fit results.

ISGRI rev	Γ	$E_{\rm Fold}$[a] (keV)	$E_{\rm Cut}$[b] (keV)	Flux[c]
1261	1.55 ± 0.06	273.6 ± 94.6	68.9 ± 12.6	2.82 ± 0.07
1262	1.45 ± 0.20	<110.5	>178.6	2.63 ± 0.09
1263	1.56 ± 0.06	255.9 ± 82.3	65.7 ± 16.7	2.37 ± 0.04
1264	1.60 ± 0.04	220.3 ± 62.0	81.2 ± 13.4	2.30 ± 0.03
1265	1.61 ± 0.07	$33.0^{+109.1}_{-21.3}$	$140.8^{+13.2}_{-31.9}$	2.03 ± 0.11
1266	1.70 ± 0.09	–	–	2.08 ± 0.07
1267	1.74 ± 0.09	–	–	1.65 ± 0.06
1271	1.62 ± 0.14	–	–	1.11 ± 0.09
1274	1.72 ± 0.23	–	–	0.74 ± 0.24
1276	1.74 ± 0.14	–	–	0.71 ± 0.05
1277	1.84 ± 0.10	–	–	0.76 ± 0.03
1279	1.72 ± 0.10	–	–	0.97 ± 0.04
1280	1.78 ± 0.09	–	–	1.22 ± 0.04
1282	1.64 ± 0.05	131.8 ± 71.5	114.2 ± 15.4	1.83 ± 0.05

Note: [a]Folding energy in *highecut* model.
[b]Cut-off energy in *highecut* model.
[c]13–200 keV flux in units of 10^{-9} erg cm^{-2} s^{-1}.

1266–1280 because of higher exposure as well as higher flux due to the observation occurring near the peak of the X-ray flare.

For *INTEGRAL* revolutions with simultaneous *Swift* XRT data, we applied joint fits with three models: phenomenological *highec*(power+diskbb)*, and Comptonization models *compps+diskbb* and *eqpair+diskbb*. For revolutions 1261, 1263, 1264 and 1282, a cut-off is required in the power-law model fit (see Table 5). The evolution of spectral parameters related to hard X-rays is summarized in Fig. 4. In this figure, we used filled circles to represent joint fit results, and used diamonds from ISGRI-only fits for which we do not have XRT data.

At first instance, fits from the earliest five revolutions seem to have a harder photon index compared to later revolutions; however, this is an artificial result due to the presence of a cut-off in the spectra of earlier revolutions. This evolution indicates that it is likely that the data from revolutions 1266–1280 also require a high-energy cut-of; however, since it is not required by the *F*-test due to low statistics, the cut-off is not included in the fits and the resulting power-law index is softer.

The evolution of folding and cut-off energies indicate that as the flux decayed initially, the cut-off energies increased and folding energies decreased. The high-cut-off, low-folding-energy behaviour was also observed during the peak of the secondary flare during revolution 1282.

For the *compps* fits, we first let electron temperature, *y*-parameter (τ_y), and reflection fraction free. For all observations, the reflection fraction is close to zero and could not be constrained by the fits. We then fixed this parameter to zero, and fitted the spectra with electron temperature and τ_y as free parameters (see Table 5 for results). We find electron temperatures of 60–100 keV for the revolutions 1261–1264. The electron temperature at revolution 1282 is higher, but with large errors. We cannot constrain the τ_y with *compps* fits, within $\Delta\chi^2$ of 2.706, the τ_y parameter is pegged to the upper limit of 3.

For the *eqpair* fits, we started with fixing $l_{\rm nt}/l_{\rm h}$ to zero to see if the thermal electron distribution can fit the data. We only had $l_{\rm h}/l_{\rm s}$ (hard to soft compactness ratio) and τ_p free and fixed all the other parameters. After we obtained initial fits, we let reflection fraction

Table 5. Joint fit results.

		High-energy cut-off fits			
ISGRI rev	Γ	$E_{\rm Fold}$	$E_{\rm Cut}$	Flux[a]	χ^2/DOF
1261	1.61 ± 0.02	345.8 ± 113.9	74.8 ± 15.7	3.69 ± 0.05	407.4/357
1262	1.68 ± 0.03	–	–	3.422 ± 0.05	310.4/284
1263	1.58 ± 0.01	262.2 ± 83.5	68.4 ± 14.5	3.10 ± 0.07	235.0/269
1264	1.64 ± 0.03	215.8 ± 70.8	91.3 ± 18.4	3.00 ± 0.04	295.5/275
1276	1.66 ± 0.03	–	–	0.98 ± 0.05	96.4/ 88
1279	1.70 ± 0.06	–	–	1.26 ± 0.05	89.0/ 94
1280	1.72 ± 0.06	–	–	1.61 ± 0.04	122.0/111
1282	1.61 ± 0.04	129.6 ± 68.2	111.6 ± 14.1	2.30 ± 0.05	179.7/135
		Compps fits			
ISGRI rev	$kT_{\rm e}$ (keV)		τ_y		χ^2/DOF
1261	73.5 ± 13.4		$3^{+0}_{-0.93}$		409.0/358
1262	92.9 ± 23.9		$3^{+0}_{-1.60}$		317.8/283
1263	66.3 ± 8.0		$3^{+0}_{-0.62}$		239.7/270
1264	69.3 ± 11.8		$3^{+0}_{-0.89}$		295.7/276
1282	119.3 ± 60.9		$3^{+0}_{-2.16}$		187.2/136
		Eqpair fits[b]			
ISGRI rev	τ_p	$l_{\rm h}/l_{\rm s}$	$\chi^2_{\rm ther}$/DOF[c]	$l_{\rm nt}/l_{\rm h}$[d]	$\chi^2_{\rm hybr}$/DOF[e]
1261	2.06 ± 0.11	12.25 ± 1.08	406.8/357	<0.48	406.6/356
1262	1.23 ± 0.24	9.99 ± 1.12	313.1/282	>0.39	306.5/281
1263	2.03 ± 0.31	11.51 ± 1.10	240.5/269	<0.50	240.5/268
1264	1.79 ± 0.32	10.37 ± 0.93	294.2/275	<0.78	293.5/274
1282	1.32 ± 0.70	8.29 ± 1.18	185.4/135	<0.57	188.8/134

Note: [a]1–200 keV flux in units of 10^{-9} erg cm^{-2} s^{-1}.
[b]$l_{\rm bb}$ is fixed to 1, $\Gamma_{\rm inj}$ is fixed to 2.5 and Refl is fixed to 0.
[c]χ^2 of thermal electron energy distribution fits, $l_{\rm nt}/l_{\rm h} = 0$.
[d]2σ limits.
[e]χ^2 of hybrid electron energy distribution fits, $l_{\rm nt}/l_{\rm h}$ is a free parameter.

vary. Like the *compps* case, for all revolutions, the fits resulted in reflection fractions close to zero. We fixed it to zero and repeated the fits. The results are given in Table 5.

We then tested whether a hybrid electron energy distribution provides better fit to the data. We made $l_{\rm nt}/l_{\rm h}$ a free parameter and fixed $\Gamma_{\rm inj}$ to 2.5. While the fits cannot constrain the $l_{\rm nt}/l_{\rm h}$ parameter well enough to rule out non-thermal plasma, we consistently obtain low values of $l_{\rm nt}/l_{\rm h}$ for all revolutions, except revolution 1262. The 2σ limits for this parameter are given in Table 5. Except revolution 1262, $l_{\rm nt}/l_{\rm h}$ values are consistent with zero, and the $l_{\rm h}/l_{\rm s}$ and τ_p parameters for the non-thermal fits are very similar to the thermal fits. Therefore, in Table 5, we only show thermal fit results for these parameters.

4 DISCUSSION

4.1 The origin of the flare in X-rays and optical

The secondary flare is clearly visible at hard-X-ray and optical wavelengths, starting around MJD ∼56380 and ending by MJD ∼56440 (Fig. 2). Flares in optical and infrared are common during the decays of GBHTs. These flares can be attributed to formation of compact jets (Kalemci et al. 2013, and references therein), synchrotron radiation from hot accretion flows (Poutanen & Veledina 2013, and references therein) and enhanced mass accretion from outer disc or the companion as a response to heating from primary (Augusteijn, Kuulkers & Shaham 1993; Ertan & Alpar 2002; Zurita et al. 2002).

Being likely a failed outburst, Swift J1745−26 did not go through a soft state, and even at the beginning of the decay, the radio emission from the compact jet was present as indicated by the flat to inverted radio spectra from ATCA observations (see Fig. 2). While the radio emission is present, whether we could observe infrared emission at the same time depends on the evolution of the break in the jet SED. In MAXI J1836–194, which also performed a failed outburst, the jet never quenched at radio frequencies, but the break in the spectrum between optically thin and partially self-absorbed (flat/inverted) synchrotron emission moved from the mm regime to the infrared regime as the source made a transition back to the HS. This indicated an increase in the jet power as the source entered the HS, resulting in a flare in the infrared and optical emission (Russell et al. 2013a, 2014). Similar evolution may be occurring in Swift J1745−26, whereby the late flare could be a result of break frequency moving towards the infrared. However, the flare in MAXI J1836–194 peaked within a few days of the transition to the HS, as did the flare of GX 339−4 in 2011 (Corbel et al. 2013b). Kalemci et al. (2013) have shown that the infrared flares usually peak about 10–20 d after the source has fully entered the HS. The late optical and X-ray re-brightening of Swift J1745−26 occurred about 100 d after the transition to the HS, which is therefore substantially delayed compared to these synchrotron jet flares. Unfortunately, we do not have optical coverage within days of the transition to the HS, so we do not know if there was an additional optical/infrared flare at that time. The hot accretion¿ $\frac{1}{2}$ flow is also an unlikely explanation for the flare, as throughout the decay that lasts for more than 100 d, there is no significant change in the properties of hard X-rays, and it is difficult to explain why the synchrotron emission suddenly turns on 80 d after the start of the decay.

Independent of the emission mechanism, a late flare could be caused by enhanced mass accretion in response to a previous heating event, which could in principal boost all accretion components at late times (disc emission, hot flow or jet). The event that triggered the enhanced mass accretion for Swift J1745−26 could be the initial outburst that peaked around MJD 56190, or it could be the increase in the hard X-rays observed between MJD 56260 and MJD 56270 which likely correspond to a transition from an intermediate state to the HS (Curran et al. 2014). Being observed in both X-rays and optical also support that the origin of this flare is enhanced mass accretion. For such a scenario, one would expect the X-rays to lag the optical flare (Ertan & Alpar 2002); however, the optical coverage is insufficient to test this prediction.

Such simultaneous X-ray/OIR flares are observed in other sources. XTE J1752−223 is such a case in which a late flare occurred ∼55 d after the transition to the HS. Russell et al. (2012) measured the SED optical to X-ray spectral index during the flare to be -1.0 ± 0.3, which is consistent with synchrotron emission from a compact jet. A detailed investigation of SMARTS light-curves in the *H* and *I* bands show that apart from the large flare with simultaneous enhancement in the OIR and X-rays, there is an earlier, smaller flare observed close to the first detection of the compact core with the VLBA (Chun et al. 2013). Kalemci et al. (2013) interpreted this smaller flare as corresponding to the formation of compact jet, and large simultaneous X-ray/OIR flare as caused by enhanced mass accretion.

Similar behaviour is observed during the decay of GX 339−4 in its 2007 outburst. The OIR flare that started on MJD 54241 is interpreted as formation of the compact jet in Kalemci et al. (2013). The OIR flare, instead of decaying within a few tens of days as in other outbursts of GX 339−4, 4U 1543−47and XTE J1550−564 (Buxton et al. 2012; Kalemci et al. 2013), lasted for more than 100 d (Dincer et al. 2008). An X-ray flare starts around MJD 52460, which corresponds to a break and a slight increase in the *H*-band flux (see fig. 3 of Dincer et al. 2008).

Based on these observations, we claim that there are two types of secondary maxima of OIR emission in GBHTs during outburst decays. During the formation of the compact jets, combination of increase in jet power and/or increase in the frequency of the SED break results in an increase in the OIR emission. These OIR flares are not accompanied by an increase in X-ray flux, and their properties are discussed in detail in Kalemci et al. (2013). The second type of OIR flare is caused by increased mass accretion due to a previous heating event, and these type of flares are accompanied by an increase in X-ray flux. For some sources, only one type flare is observed, and for others (like GX 339−4 in 2007 and XTE J1752−223) both can be observed during the same outburst.

While the underlying mechanism causing the simultaneous secondary X-ray/OIR flares might be the increased mass accretion for these sources, this does not by itself reveal the emission mechanism. Since the source is in the HS at this time, a mass increase in the disc going towards the black hole may increase the flux of all the accretion components: inner disc, hot flow and the jet. We might obtain some clues about the emission mechanism by investigating the evolution of X-ray spectra as discussed in the next section.

4.2 High-energy behaviour of the source

Thanks to the wide field of view of the *INTEGRAL* ISGRI instrument, and pointed observations with *Swift* XRT, we were able to analyse the broad-band spectral evolution of the source at the beginning of the decay (revolutions 1261–1264) and at the peak of the flare (revolution 1282). We have shown that five revolutions having ISGRI data with good statistical quality require a cut-off in the fit, and we have some evidence (from Γ) that several others probably have a cut-off.

4.2.1 *High-energy breaks and jets*

Both of the sources we observed with our *INTEGRAL* programme, XTE J1752−223 and Swift J1745−26, show presence of a break in the hard-X-ray spectrum while the jets are present. This was in contrast to our earlier results from the HEXTE data that indicate disappearance of breaks while the jet turns on. Suspecting that the disappearance of the break is an artefact of the quality of the data, we decided to check the spectra of 4U 1543−47 and H1743−322 during their decays to find which combinations of cut-off and folding energies are statistically acceptable. For both 4U 1543−47 and H1743−322, we found the observations with the best statistics, and multiplied the existing fit with the *highecut*. As reported earlier in Kalemci et al. (2005, 2006a), the addition of the break into the spectrum is not statistically significant. We then used *steppar* in XSPEC and varied the cut-off and folding energies and recorded the χ^2 values. We plotted contours of 5 and 1 per cent levels for which the given folding and cut-off values are acceptable. We show the H1743−322 ObsID 80137-02-01-01 result as an example in Fig. 6 because it had ∼6 ks of exposure with *RXTE*, and had the best statistics for fitting the spectrum. Even at the 5 per cent level, a large parameter space of folding and cut-off energies can fit the data. To illustrate this point further, we placed the cut-off and break energy combinations of Swift J1745−26 from this work, and all of these combinations would lead to an acceptable fit for the example spectrum of H1743−322 that we discuss. For all other observations with *RXTE* (including observations for 4U 1543−47), the statistics are even worse than the example given, and basically all combinations of cut-off and folding energies are acceptable, except low cut-off (<50 keV) and low-folding-energy (<100 keV) combinations. Therefore, spectra taken with HEXTE on *RXTE* provide insufficient quality to characterize cut-offs during the decay for typical hard-X-ray fluxes. Long *INTEGRAL* monitoring observations are required to understand the relation between the compact jet formation and hard-X-ray behaviour.

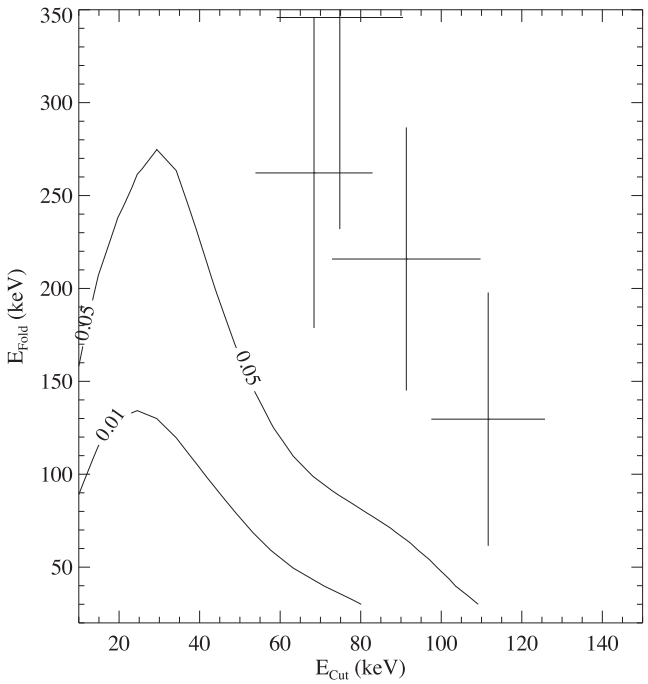

Figure 6. Contours of 5 and 1 per cent confidence levels for goodness of fit for the long H1743−322 observation taken with *RXTE* when cut-off and folding energies are varied in the fit. The Swift J1745−26 cut-off and folding energies with errors are over plotted.

We can compare the behaviour of the spectral breaks of Swift J1745−26 with different sources. For 4U 1543−47, with the formation of the jet, the folding energy and/or the cut-off energy must have increased. For H1743−322, no break was necessary in the fit before the presence of compact jets, and this trend continued after the compact jet is observed, so we do not know the evolution, but we can say that even if there is a break, the cut-off and/or folding energies must be high when the compact jet is present. For Swift J1745−26, we observed an increase in the cut-off energy as the decay progressed during the outburst decay, but we also observed a decrease in the folding energy, resulting in a sharp break in the spectrum. The situation is quite different for XTE J1752−223 where we measured a cut-off energy of $25.3^{+7.3}_{-7.6}$ keV and a folding energy of 236^{+42}_{-32} keV (Chun et al. 2013) indicating a smooth, gradual break at high energies. This observation took place when the compact jet was first observed with the VLBA, but before the large secondary flare. Overall, the behaviour of Swift J1745−26 and XTE J1752−223 for which we have high-quality *INTEGRAL* data do not support the argument that the high-energy breaks disappear as the jets turn on.

High-energy breaks as discussed in this work are a common feature in models invoking both Comptonization and synchrotron as the source of emission. For the model discussed in Pe'er & Markoff (2012), the electrons at the jet base characteristically produce a power law with a photon index of around 1.5 and a break at higher energies. The location of the break is determined by the acceleration mechanism whose details are uncertain. While Pe'er & Markoff (2012) model can roughly reproduce the spectra for both earlier and later revolutions of Swift J1745−26 (Peer, personal communication), it cannot place strong constraints on the physical parameters yet.

Recently, based on a broad-band observation taken at MJD 56446 at the end of the secondary flare (the last i' data in Fig. 2), Grebenev et al. (2014) claimed that emission at the time may be dominated by jet emission since a single power law can fit the entire SED from optical to gamma-rays. They first take the optical and a single *Swift* BAT flux, and fitted them with a single power law by modifying the $N_{\rm H}$. Then they added *Swift* XRT spectra taken 10 d earlier (last observation in Table 2), and showed that the single power law with an $N_{\rm H}$ of $1.205 \pm 0.026 \times 10^{22}$ atoms cm^{-2} found from the optical to BAT fit also fits the XRT data. While this result seems intriguing, we do not think that the quality of the data is sufficient for arriving at strong conclusions about the emission mechanism. We have also analysed the same XRT data using their absorption model, and found that the fit gives $N_{\rm H} = 1.44 \pm 0.29 \times 10^{22}$ atoms cm^{-2}. Therefore, errors on both the power-law index and $N_{\rm H}$ are quite large, and it is not surprising that a single power law passes through all XRT data.

4.2.2 *Comptonization models*

The behaviour of hard X-rays can be well explained by Comptonization for Swift J1745−26. The thermal Comptonization model *compps* fits provide reduced χ^2 values close to 1. Finally, all revolutions, except revolution 1262, can be fitted with the *eqpair* model without requiring a hybrid electron plasma. Therefore, except revolution 1262, the high-energy behaviour of the source is consistent with thermal Comptonization of disc photons. Fig. 5 shows that phenomenological and physical fits all represent the data very well (which is not surprising; see discussion in Coppi 1999).

Even for revolution 1262 a thermal Comptonization model cannot be ruled out given the very small improvement of χ^2 of the hybrid case to that of the thermal case (see Table 5). The *compps* still provides an acceptable fit (reduced χ^2 of 1.123). We added a hard power law to *compps* fit (following Joinet et al. 2007) to test the presence of additional components due to non-thermal Comptonization. The fitted power-law index was ∼1 (not constrained), and the improvement in the χ^2 was marginal (with an *F-test* chance probability of 0.008).

While non-thermal electron energy distributions are commonly required in the intermediate and sometimes in the soft states (Gierliński et al. 1999; Malzac et al. 2006; Del Santo et al. 2008), they are rarely required in the HS, and all claims of non-thermal electron distributions in the HS are during bright HS at the outburst rise (McConnell et al. 2000; Caballero García et al. 2007; Joinet et al. 2007; Droulans et al. 2010). Thanks to our *INTEGRAL* observing programme, now we obtained high-quality data extending above 300 keV for two sources in the HS during the decay, XTE J1752−223 (Chun et al. 2013) and Swift J1745−26, and for both sources fits are consistent with thermal Comptonization. Continuing dedicated *INTEGRAL* observations of GBHTs during outburst decays is very important to establish patterns in the high-energy behaviour, and to compare these patterns with the behaviour during outburst rise.

5 SUMMARY

We characterized the multiwavelength evolution of Swift J1745−26 during the decay of the 2013 outburst using X-ray data from *INTEGRAL* ISGRI, JEM-X and *Swift* XRT optical observations taken at FTS and RTT150 and radio observations of ATCA. We fit the X-ray spectra with thermal and hybrid Comptonization models as well as phenomenological models. Our main findings can be summarized as follows.

(i) We concluded that the physical origin of a flare observed both in optical and X-rays ∼170 d after the peak of the outburst that lasted for ∼50 d is enhanced mass accretion in response to an earlier heating event.

(ii) We showed that a high-energy break is needed in the spectra, and for the joint ISGRI–XRT fits, the cut-off energy increased from 75 to 112 keV while the folding energy decreased from 350 to 130 keV as the decay progresses.

(iii) We investigated the claim that high-energy cut-offs disappear with the compact jet turning on during outburst decays, and showed that spectra taken with HEXTE on *RXTE* provide insufficient quality to characterize cut-offs during the decay for typical hard-X-ray fluxes. Data taken with *INTEGRAL* do not support the claim of disappearance of spectral breaks.

(iv) We found that for the entire decay (including the flare) the X-ray spectra are consistent with thermal Comptonization, but jet synchrotron origin cannot be ruled out.

ACKNOWLEDGEMENTS

EK and TD acknowledge TÜBİTAK 1001 Project 111T222, the EU FP7 Initial Training Network Black Hole Universe, ITN 215212. JAT acknowledges partial support from NASA Astrophysics Data Analysis Programme grant NNX11AF84G and *Swift* Guest Observer grant NNX13AJ81G. The FTS is maintained and operated by Las Cumbres Observatory Global Telescope Network. DMR acknowledges support from a Marie Curie Intra European Fellowship within the 7th European Community Framework Programme (FP7) under contract no. IEF 274805. TMB acknowledges support from INAF PRIN 2012-6. EK thanks J. Chenevez, C. A. Oxborrow and N. Westergaard of DTU Space for JEM-X analysis tips, and A. Pe'er and S. Markoff for valuable discussions on hard-X-ray contribution from jets. TG acknowledges support from Bilim Akademisi – The Science Academy, Turkey under the BAGEP Programme.

REFERENCES

Augusteijn T., Kuulkers E., Shaham J., 1993, A&A, 279, L13
Belloni T. M., 2010, in Belloni T., ed., Lecture Notes in Physics, Vol. 794, The Jet Paradigm. Springer-Verlag, Berlin, p. 53
Belloni T. et al., 2012, Astron. Telegram, 4450
Blandford R. D., Konigl A., 1979, ApJ, 232, 34
Brocksopp C., Bandyopadhyay R. M., Fender R. P., 2004, New Astron., 9, 249
Buxton M., Bailyn C. D., 2004, ApJ, 615, 880
Buxton M., Bailyn C. D., Capelo H., Chatterjee R., Dincer T., Kalemci E., Tomsick J. A., 2012, AJ, 143, 130
Caballero García M. D. et al., 2007, ApJ, 669, 534
Cadolle Bel M. et al., 2004, A&A, 426, 659
Capitanio F., Belloni T., Del Santo M., Ubertini P., 2009, MNRAS, 398, 1194
Chun Y. Y. et al., 2013, ApJ, 770, 10
Coppi P. S., 1999, in Poutanen J., Svensson R., eds, ASP Conf. Ser. Vol. 161, High Energy Processes in Accreting Black Hole. Astron. Soc. Pac., San Francisco, p. 375
Corbel S., Fender R. P., 2002, ApJ, 573, L35
Corbel S., Fender R. P., Tzioumis A. K., Nowak M., McIntyre V., Durouchoux P., Sood R., 2000, A&A, 359, 251
Corbel S., Edwards P., Tzioumis T., Coriat M., Fender R., Brocksopp C., 2012, Astron. Telegram, 4410
Corbel S., Coriat M., Brocksopp C., Tzioumis A. K., Fender R. P., Tomsick J. A., Buxton M. M., Bailyn C. D., 2013a, MNRAS, 428, 2500
Corbel S. et al., 2013b, MNRAS, 431, L107
Coriat M., Corbel S., Buxton M. M., Bailyn C. D., Tomsick J. A., Körding E., Kalemci E., 2009, MNRAS, 400, 123
Courvoisier T. J.-L. et al., 2003, A&A, 411, L53
Cummings J. R., Gronwall C., Grupe D., Krimm H. A., Markwardt C. B., Palmer D. M., Sbarufatti B., Stamatikos M., 2012, GCN Circ., 13775
Curran P. A. et al., 2014, MNRAS, 437, 3265
de Ugarte Postigo A., Sanchez-Ramirez R., Munoz-Darias T., Gorosabel J., Thoene C. C., Cabrera-Lavers A., 2012, Astron. Telegram, 4388
Del Santo M., Malzac J., Jourdain E., Belloni T., Ubertini P., 2008, MNRAS, 390, 227
Dincer T., Kalemci E., Tomsick J. A., Buxton M., 2008, in Kalemci E., ed., Proc. VII Microquasar Workshop: Microquasars and Beyond, PoS(MQW7)061
Dinçer T., Kalemci E., Tomsick J. A., Buxton M., Bailyn C., Corbel S., 2012, ApJ, 753, 55
Droulans R., Belmont R., Malzac J., Jourdain E., 2010, ApJ, 717, 1022
Ertan Ü., Alpar M. A., 2002, A&A, 393, 205
Fender R. P., 2001, MNRAS, 322, 31
Fender R., 2010, in Belloni T., ed., Lecture Notes in Physics, Vol. 794, The Jet Paradigm. Springer-Verlag, Berlin, p. 115
Fender R. P., Gallo E., 2014, Space Sci. Rev., 183, 323
Ferrigno C., Bozzo E., Del Santo M., Capitanio F., 2012, A&A, 537, L7
Gierliński M., Zdziarski A. A., Poutanen J., Coppi P. S., Ebisawa K., Johnson W. N., 1999, MNRAS, 309, 496
Gilfanov M., 2010, in Belloni T., ed., Lecture Notes in Physics, Vol. 794, The Jet Paradigm. Springer-Verlag, Berlin p. 17
Grebenev S. A., Sunyaev R. A., 2012, Astron. Telegram, 4401
Grebenev S. A., Prosvetov A. V., Burenin R. A., 2014, Astron. Lett., 40, 171
Hjellming R. M., Johnston K. J., 1988, ApJ, 328, 600
Homan J., Wijnands R., van der Klis M., Belloni T., van Paradijs J., Klein-Wolt M., Fender R., Méndez M., 2001, ApJS, 132, 377

Jain R. K., Bailyn C. D., Orosz J. A., McClintock J. E., Remillard R. A., 2001, ApJ, 554, L181
Joinet A., Jourdain E., Malzac J., Roques J. P., Corbel S., Rodriguez J., Kalemci E., 2007, ApJ, 657, 400
Joinet A., Kalemci E., Senziani F., 2008, ApJ, 679, 655
Kalemci E., Tomsick J. A., Buxton M. M., Rothschild R. E., Pottschmidt K., Corbel S., Brocksopp C., Kaaret P., 2005, ApJ, 622, 508
Kalemci E., Tomsick J. A., Rothschild R. E., Pottschmidt K., Corbel S., Kaaret P., 2006a, ApJ, 639, 340
Kalemci E., Tomsick J. A., Rothschild R. E., Pottschmidt K., Migliari S., Corbel S., Kaaret P., 2006b, Proc. VI Microquasar Workshop: Microquasars and Beyond, PoS(MQW6)012
Kalemci E., Dincer T., Tomsick J. A., Buxton M. M., Bailyn C. D., Chun Y. Y., 2013, ApJ, 779, 95
Lewis F., Russell D. M., Fender R. P., Roche P., Clark J. S., 2008, Proc. VII Microquasar Workshop: Microquasars and Beyond, PoS(MQW7)069
McClintock J. E., Remillard R. A., 2006, in Lewin W. H. G., van der Klis M., eds, Compact Stellar X-ray Sources. Cambridge Univ. Press, Cambridge, p. 157
McConnell M. L. et al., 2000, ApJ, 543, 928
Maitra D., Markoff S., Brocksopp C., Noble M., Nowak M., Wilms J., 2009, MNRAS, 398, 1638
Makishima K., Maejima Y., Mitsuda K., Bradt H. V., Remillard R. A., Tuohy I. R., Hoshi R., Nakagawa M., 1986, ApJ, 308, 635
Malzac J. et al., 2006, A&A, 448, 1125
Markoff S., Falcke H., Fender R., 2001, A&A, 372, L25
Markoff S., Nowak M. A., Wilms J., 2005, ApJ, 635, 1203
Miller-Jones J. C. A., Sivakoff G. R., 2012, Astron. Telegram, 4394
Miyakawa T., Yamaoka K., Homan J., Saito K., Dotani T., Yoshida A., Inoue H., 2008, PASJ, 60, 637
Motta S., Belloni T., Homan J., 2009, MNRAS, 400, 1603
Muñoz-Darias T. et al., 2013, MNRAS, 432, 1133
Nowak M. A. et al., 2011, ApJ, 728, 13
Pe'er A., Markoff S., 2012, ApJ, 753, 177
Poutanen J., Svensson R., 1996, ApJ, 470, 249
Poutanen J., Veledina A., 2013, Space Sci. Rev., 183, 61
Rau A., Knust F., Kann D. A., Greiner J., 2012, Astron. Telegram, 4380
Reynolds M. T., Miller J. M., 2013, ApJ, 769, 16
Russell D. M., Maitra D., Dunn R. J. H., Markoff S., 2010, MNRAS, 405, 1759
Russell D. M., Miller-Jones J. C. A., Maccarone T. J., Yang Y. J., Fender R. P., Lewis F., 2011, ApJ, 739, L19
Russell D. M. et al., 2012, MNRAS, 419, 1740
Russell D. M. et al., 2013a, ApJ, 768, L35
Russell D. M., Lewis F., Munoz-Darias T., Kalemci E., 2013b, Astron. Telegram, 5084
Russell T. D., Soria R., Miller-Jones J. C. A., Curran P. A., Markoff S., Russell D. M., Sivakoff G. R., 2014, MNRAS, 439, 1390
Sbarufatti B. et al., 2012, Astron. Telegram, 4383
Sbarufatti B., Kennea J. A., Stroh M. C., Burrows D. N., Evans P. A., Beardmore A. P., Krimm H. A., Gehrels N., 2013, Astron. Telegram, 4782
Soleri P. et al., 2013, MNRAS, 429, 1244
Tomsick J. A., Del Santo M., Belloni T., 2012, Astron. Telegram, 4393
Veledina A., Poutanen J., Vurm I., 2013, MNRAS, 430, 3196
Verner D. A., Ferland G. J., Korista K. T., Yakovlev D. G., 1996, ApJ, 465, 487
Vovk I. et al., 2012, Astron. Telegram, 4381
Wilms J., Allen A., McCray R., 2000, ApJ, 542, 914
Zurita C. et al., 2002, MNRAS, 334, 999

This paper has been typeset from a TEX/LATEX file prepared by the author.